Cement and Concrete Research 108 (2018) 38–45

Contents lists available at ScienceDirect

Cement and Concrete Research

journal homepage: www.elsevier.com/locate/cemconres

A high-pressure X-ray diffraction study of the crystalline phases in calcium aluminate cement paste

Guoqing Geng[a,*], Jiaqi Li[a], Yang Zhou[a,b], Lin Liu[a,c], Jinyuan Yan[d], Martin Kunz[d], Paulo J.M. Monteiro[a,e]

[a] Department of Civil and Environmental Engineering, University of California, Berkeley, CA 94720, United States
[b] Department of Material Science and Engineering, Southeast University, Nanjing, Jiangsu 211189, China
[c] College of Civil and Transportation Engineering, Hohai University, Nanjing, Jiangsu 210098, China
[d] Advanced Light Source, Lawrence Berkeley National Laboratory, Berkeley, CA 94720, United States
[e] Material Science Division, Lawrence Berkeley National Laboratory, Berkeley, CA 94720, United States

ARTICLE INFO

Keywords:
Calcium aluminate cement (D)
Mechanical properties (B)
High-pressure X-ray diffraction
Crystal structure (B)

ABSTRACT

Calcium aluminate cement (CAC) has wide application in civil engineering and castable refractory materials. The main binding phases of hardened CAC paste, $CaO{\cdot}Al_2O_3{\cdot}10H_2O$ (CAH_{10}), inevitably converts to $2CaO{\cdot}Al_2O_3{\cdot}8H_2O$ (C_2AH_8), $3CaO{\cdot}Al_2O_3{\cdot}6H_2O$ (C_3AH_6) and $Al(OH)_3$ (AH_3), leading to a significant change in the mechanical properties of the CAC matrix. This work investigates the mechanical properties of the main crystalline components in hydrated and/or converted CAC systems, using synchrotron-radiation-based high-pressure X-ray diffraction. The anisotropic deformations of $CaAl_2O_4$ (CA), CAH_{10} and C_3AH_6 along each crystallographic direction are investigated, along with their bulk moduli. The density-driven stiffening hypothesis is validated for the studied phases and other cement-based minerals. An atom-scale topological analysis is proposed to explain the unusually high stiffness of CAH_{10}. The results provide fundamental information to understand the mechanical properties of single cement-based phases at molecular level, and enable predicting the changing mechanical properties of converted CAC matrix using homogenization models.

1. Introduction

Calcium aluminate cement (CAC) is an important member of the hydraulic cement family. In contact with water, its main component CA (cement chemistry notation, C=CaO and A=Al_2O_3) hydrates rapidly, accompanied by a quick heat-release and a fast strength-development. Such cementing performance leads to the wide application of CAC in civil engineering practices [1,2]. However since the 1970s the concrete community suggested to limit the use of CAC in structural application, due to increasing numbers of failure reports of CAC concrete over the long-term service life [1–4]. In recent years, standards have been proposed to guide the proper use of CAC concrete in civil engineering [2,5]. Nonetheless, CAC continues to be applied in infrastructures that face severe chemical and abrasive load [4]. It is also widely used in producing castable refractory linings [6].

The hydration path of CA is strongly temperature-dependent. It hydrates to form CAH_{10} (H=H_2O) when the curing temperature is below 15–20 °C, whereas C_2AH_8 + AH_3 is the product when the temperature is between 20 and 30 °C. In ordinary service condition, these phases account for the rapid early age strength development. However, CAH_{10} and C_2AH_8 inevitably convert to C_3AH_6 + AH_3, as the latter phases are thermodynamically more favorable. This conversion reaction significantly accelerates when temperature is higher than 30 °C [7–10]. A recent micro-spectroscopic study reported that CAH_{10} easily converts to C_2AH_8 via a solid-state-reaction path where the ion redistribution happens in a very short range inside the CAH_{10} crystals, resulting in a nanometer scale C_2AH_8 sheet structure [10,11]. The formation of C_3AH_6 is, on the contrary, more likely through solution. Since C_3AH_6 and AH_3 have higher densities than CAH_{10} and C_2AH_8, the conversion reaction significantly increases the porosity of the hardened matrix, and is therefore the major cause of the strength-loss of CAC concrete.

Homogenization modeling schemes have been proved successful in predicting the mechanical properties, such as elastic modulus, of hardened Portland cement (PC) matrix [12–14]. Such schemes require two types of input: 1) the microstructural information of each phase, i.e. the volume fraction, shape and size of the a single phase domain; 2) the mechanical property of each single phase. Experimental investigations

* Corresponding author.
E-mail address: guoqing_geng@berkeley.edu (G. Geng).

https://doi.org/10.1016/j.cemconres.2018.03.004
Received 13 September 2017; Received in revised form 23 January 2018; Accepted 14 March 2018

of the mechanical property of CAC-based concrete [15,16] and refractory linings [17,18] have been reported, however a homogenization modeling based on the structural evolution has yet to be proposed. To enable such modeling, the modulus of individual phases in the CAC matrix is needed, yet such information has not been systematically reported by the cement and concrete research community. It is also of mineralogical and materials science interest to understand the molecular-scale mechanism of how these minerals deform under mechanical loading.

Synchrotron-radiation-based high-pressure X-ray diffraction (HP-XRD) is reported to be a reliable method to probe the mechanical property of (nano)crystalline cement-based phases. Compared with nano-indentation which measures the average information of solid and porosity at the microscale, HP-XRD has the advantage of measuring the intrinsic mechanical property of crystalline solids that contains no contribution from inter-particle pores. It also provides atomistic scale mechanism of the deformation of crystals [20–24]. The earlier HP-XRD study [25] and molecular calculation [26] of C_3AH_6 reported bulk modulus of 66 ± 4 GPa and 56.3 GPa, respectively. Both did not observe any pressure-induced phase transition. A high-pressure single crystal X-ray diffraction study reported the phase transition from *Ia3d* to *I-43d* symmetry at 5 GPa, [27] which is later confirmed by high-pressure neutron powder diffraction and infrared spectroscopic study [28]. The reported high-pressure diffraction work on CA mainly focuses on the chemical environmental evolving with pressure and temperature increase, yet the lattice deformation is rarely reported [32,33]. There is no existing report on the HP-XRD work of CAH_{10}.

In the present work, we aim to investigate the mechanical properties of the three major components in hardened CAC matrix, i.e. CA, CAH_{10} and C_3AH_6, using Synchrotron-radiation-based HP-XRD. The significance of the present study is twofold: 1) to provide the mechanical properties of the single phase as input for homogenization modeling of the macro-scale mechanical behavior of CAC-based matrix, which dynamically evolves via hydration and the conversion reaction; 2) to add to the basic understanding of the molecular-scale mechanism of the deformation of cement-based minerals.

2. Materials and methods

2.1. Materials

The CA and C_3AH_6 were provided by *Mineral Research Processing Cie*. Pure CAH_{10} crystals were prepared as described in the published work [9,10]. In brief, CA was mixed with deionized water with a water-to-solid ratio of 10, which was then cured at 8 ± 2 °C for seven days, followed by vacuum-filtering in a N_2-protected glove box. The CAH_{10} solids were then stored at 5 ± 1 °C until the X-ray diffraction measurement. These phases were verified by a *PANalytical X'Pert Pro*^{TR} diffractometer using a Co anode.

The crystal structure of CAH_{10} is hexagonal, with space group $P6_3/m$, and lattice parameter $a = b$ ~16.3 Å, c ~8.3 Å [29,30]. Under ambient condition, C_3AH_6 is commonly known and described as the garnet-mineral katoite, i.e. the OH-analogue of grossular. It has cubic symmetry with space group *Ia*-3d and lattice parameter $a = b = c$ ~12.6 Å [31]. There is no other polymorph of CAH_{10} or C_3AH_6 reported under ambient conditions. CA has at least three reported polymorphs as a function of temperature and pressure, and they may be retained in ambient condition after a quenching process [32–35]. From a lab XRD data, the CA used in this study best-fits the structure reported by Ref. [34], i.e. monoclinic space group $P\ 2_1/n$, with a ~8.7 Å, b ~8.1 Å, c ~15.2 Å, and β ~90.2°.

2.2. Methods

The HP-XRD experiment was conducted at beamline 12.2.2 of the Advanced Light Source (ALS) at the Lawrence Berkeley National Laboratory (LBNL), [36] using a BX90 diamond anvil cell [37]. A 250 μm steel gasket was pre-indented to 80 μm thickness, and a 150 μm diameter hole was drilled into the pre-indentation using a laser mill. Sample powders, together with one ruby sphere (diameter 3–5 μm), were placed into the whole to fill about half the empty space, followed by a complete fill with a drop of liquid pressure medium (methanol: ethanol = 4:1 by volume). With tunable external loading values, all the solid phases in the chamber are subjected to hydrostatic pressure in the order of several GPa, which is precisely measured via the florescence signal of the ruby particle [38]. For each sample, 6–9 diffraction patterns were collected from ambient pressure up to 9–12 GPa, using synchrotron X-ray (wavelength ~0.49755 Å) as the incident beam.

The 2D diffraction pattern were integrated to diffractograms using *Dioptas* software [39]. For each sample, the positions of the strong and isolated diffraction peaks were tracked as functions of applied pressure, using the *XFIT* code [40]. The peak positions were then used to refine the lattice parameters under each pressure value, using the CELREF code [41]. This approach is applicable in the present study since the samples yield strong diffraction [22]. The pressure induced volumetric change is related to the bulk modulus by the second-order Birch-Murnaghan equation of state (BM-EoS) [42]:

$$P = \frac{3}{2}K_0\left[\left(\frac{V}{V_0}\right)^{-\frac{7}{3}} - \left(\frac{V}{V_0}\right)^{-\frac{5}{3}}\right] \quad (1)$$

where V_0 is the initial unit cell volume at ambient pressure; V is the unit cell volume at pressure P; K_0 is the bulk modulus at ambient pressure. With the volumetric strain defined as $\varepsilon_V = 1\text{-}V/V_0$, Eq. (1) is written as:

$$P = \frac{3}{2}K_0\left[(1-\varepsilon_V)^{-\frac{7}{3}} - (1-\varepsilon_V)^{-\frac{5}{3}}\right] \quad (2)$$

Due to the limited experiment time available at synchrotron facilities, the first probed pressure value needs to be noticeable via ruby calibration, which is slightly higher than ambient condition. We use the diffractograms under this pressure value (~0.2 GPa) to refine the ambient lattice parameters of CAH_{10} and C_3AH_6. Under the second-order BM-EoS, this leads to a deviation below 1 GPa in bulk modulus, which is smaller than the estimated uncertainty (~2 GPa), and is therefore considered acceptable. It will be later shown that the refined volumes under ~0.2 GPa are different from the reported ambient values by a negligible amount (smaller than refinement uncertainty). The first probed pressure for CA (3.5 GPa) is much higher than the ambient condition, therefore its ambient lattice parameters are refined from lab-XRD data.

3. Results

3.1. Diffractogram as a function of the applied hydrostatic pressure

The powder diffractograms of CA under increasing hydrostatic pressure are shown in Fig. 1. Note that the ambient pressure (0 GPa) data was not collected using HP-XRD and the lab XRD data is used instead. At ambient pressure, the strongest diffraction of CA is at $1/d$ ~0.337 Å^{-1}, corresponding to the merged diffraction of the (123) and (220) peaks. These two peaks maintain the strongest diffraction along with the increased pressure. To the right-hand-side of the strongest diffraction, there exists a group of diffractions with $1/d$ ranging from 0.39 to 0.42 Å^{-1}; and to the left-hand-side there are several isolated peaks corresponding to the diffraction of individual Miller indices, as labeled by the red dashed lines in Fig. 1.

There is a clear peak position drifting as the pressure increases, since the lattice structure is compressed from all directions. The shortening of the interplanar distance thus shifts the diffraction peaks to the direction of increasing $1/d$. As the hydrostatic pressure increases, all diffraction peaks tend to decrease in their absolute intensities, accompanied by a significant broadening of the half peak width. This

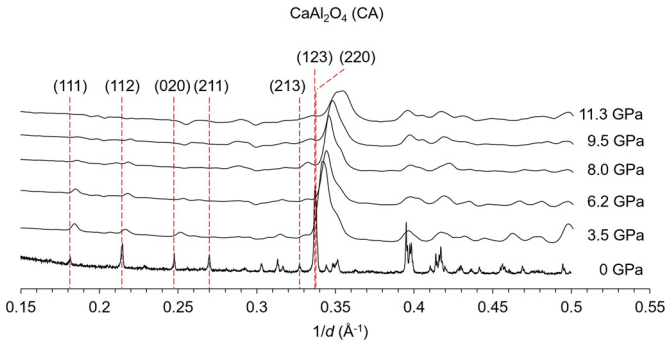

Fig. 1. The diffractograms of CA measured under increasing hydrostatic pressure. Peaks that are marked with red dashed lines are used to refine the lattice parameters. (For interpretation of the references to color in this figure legend, the reader is referred to the web version of this article.)

peak-broadening is due to the increasing degree of stress-induced structural disorder at elevated pressure, [19] which is a frequently observed phenomenon in HP-XRD experiment [20,21,23,43]. When diffraction peaks are close to each other, they may merge into one broad hump at higher pressure values. To deconvolute the (123) and (220) peak, the *XFIT* code is used and the only input information is the number of peaks [40]. No other constraints (e.g. peak intensity ratios) are introduced in order to minimize the amount of artefacts. However, no attempt was made to deconvolute the group of peaks with ambient $1/d$ ranging from 0.39 to 0.42 $Å^{-1}$, due to the large number of merged peaks. Apart from the peak broadening, the emergence of new diffraction peaks are not observed as pressure increases, indicating no reconstructive phase transition.

To refine the lattice parameters of CA at each pressure value, we used the monoclinic structure with space group $P2_1/n$ [34]. A change of crystal symmetry would often result in new peaks being generated, which is not clearly observed here. Therefore the symmetry remains unchanged at elevated pressure values. It is also worth noticing that, the angle β (90.2°) is very close to 90°. As a result, the diffraction of CA appears rather similar to an orthorhombic structure. For example, the (111), (112) and (211) peaks are perfectly overlapped with the (−111), (−112) and (−211) peaks. As labeled in Fig. 1, seven peak positions are tracked during the pressurizing, which are then used to refine the lattice parameters using a least-square-fitting scheme embedded in the CELREF code [41]. The independent lattice parameters are determined so that the squared residues between the calculated peak positions and the experimental values are minimized. A standard error is generated for each parameter during the fitting process (Table 1). Note that the positions of some small peaks, i.e. (020) and (211), are not reliably tracked at elevated pressure [21,22]. The limitation due to the low data-to-parameter ratio is, however, not necessarily reflected by the standard error.

The diffractions of CAH_{10} under increasing pressure are shown in Fig. 2. The (100), (101) and (200) diffractions are of the dorminating intensities, and the minor diffraction peaks are clearly resolved in the magnified plots (green dash squares). Again, there is no generation of new peaks, apart from the pressure-induced broadening of existing peaks. The (101) and (200) peaks overlap to form the second strongest diffraction at $1/d$ ~0.14 $Å^{-1}$. As showing in Table 2, the ratio between $d_{(100)}$ and $d_{(200)}$ is rather consistent throughout the whole pressure range, indicating that the (200) peak is reliably differentiated from the overlap with (101) peak. There are two degrees of freedom of CAH_{10} lattice structure with space group $P6_3/m$, i.e. a and c. Therefore, the strongest diffractions at $1/d$ ~0.07 $Å^{-1}$ and 0.14 $Å^{-1}$ are sufficient to determine the lattice parameters. The results are listed in Table 2.

The evolution of the diffractograms of C_3AH_6 is similar to that of CA and CAH_{10}, as shown in Fig. 3. In the probed d-spacing range, there are several diffractions of comparable intensities. C_3AH_6 has cubic structure with only one parameter (a) to be refined, yet the labeled peaks in Fig. 3 are all tracked to yield a least-squre-fitting of a. The results are listed in Table 3. A peak with ambient $1/d$ ~0.39 $Å^{-1}$ seems splitted at elevated pressure, yet it is in fact a separation of a C_3AH_6 peak (diamond symbol in Fig. 3) and a ruby peak (inversed triangle in Fig. 3). Apart from that, we did not observe the generation of new peaks.

3.2. Axial incompressibilities and bulk moduli

In order to estimate the stiffness along each crystal axis, the applied hydrostatic pressure is plotted as a function of the shortening of each unit cell edge calculated as Biot strain $\varepsilon = 1\text{-}l/l_0$, as shown in Fig. 4(a). The l_0 and l are the unit cell edge lengths under ambient and a certain pressure value, respectively. The tangential slope of the pressure vs. Biot strain curve is, by definition, the stiffness along the studied crystal direction. The error bar of axial Biot strain is usually below 0.004, which is determined by the standard deviation of fitting the lattice parameters. This further leads to the error of volumetric strain, as shown in Tables 1–3 (usually below 0.009). The error bar of the pressure values is the uncertainty of calibrating the pressure using ruby florescence, which is near 0.2 GPa [22–24].

As shown in Fig. 4(a), CA exhibits clear anisotropy along different unit cell axis directions. Under hydrostatic pressure, the shortening of CA crystal along its b-axis is about five times the shortening along c-axis, and 2–3 times the shortening along a-axis. Therefore CA has the most rigid response along its c-axis, and the softest response along the b-axis. The CAH_{10} crystal exhibits rather isotropic deformation, with comparable shortening along its a- (b-) axis and the c-axis, until a deviation is observed at pressure higher than ~7 GPa. The stiffness of CAH_{10} along each axis is comparable with that of the softest axis of CA. The C_3AH_6 is structurally isotropic due to its cubic symmetry. Its axial incompressibility is comparable to that of CAH_{10}.

To estimate the overall bulk modulus K_0, the applied hydrostatic pressure is plotted as a function of the unit cell volumetric strains $\varepsilon_V = 1\text{-}V/V_0$, where V is the unit-cell volume at current pressure and V_0 is the volume at ambient pressure which is obtained from refining the ambient pressure XRD data. This plot is then fitted with second-order Birch-Murnaghan equation of state (BM-EoS; see Eq. (2)), as shown in Fig. 4(b)–(d). Note that the bulk modulus K_0 is the only parameter to be refined. The bulk moduli of CA, CAH_{10} are 113 ± 5 GPa and 63 ± 1 GPa, respectively. The data points for C_3AH_6 follow two different trend lines at lower and higher pressure region, which disjoint at pressure range ~5 to ~8 GPa. This is consistent with the behavior of the

Table 1
The interplanar d-spacings, the lattice parameters and unit cell volume of CA under elevated hydrostatic pressure values. The angles α and γ are fixed at 90°.

P (GPa)	Interplanar d-spacings (Å)							Refined lattice parameters								V (Å^3)	V_{error} (Å^3)
	(111)	(112)	(020)	(211)	(213)	(123)	(220)	a (Å)	b (Å)	c (Å)	a_{error} (Å)	b_{error} (Å)	c_{error} (Å)	β	β_{error}		
0	5.506	4.661	4.040	3.706	3.057	2.969	2.960	8.69	8.08	15.21	0.01	0.01	0.04	90.1°	16.8°	1067.3	3.2
3.5	5.429	4.616	3.972	–	3.023	2.926	2.910	8.58	7.93	15.12	0.02	0.01	0.05	89.9°	9.6°	1028.4	4.3
6.2	5.402	4.582	3.943	–	3.014	2.911	2.893	8.55	7.87	15.07	0.03	0.01	0.06	89.9°	12.9°	1014.4	5.6
8.0	5.372	4.572	–	–	3.009	2.898	2.887	8.58	7.80	15.05	0.03	0.03	0.07	90.1°	17.1°	1006.8	7.0
9.5	5.359	4.545	–	–	2.996	2.885	2.870	8.53	7.76	15.04	0.01	0	0.01	90.0°	2.0°	995	1.2

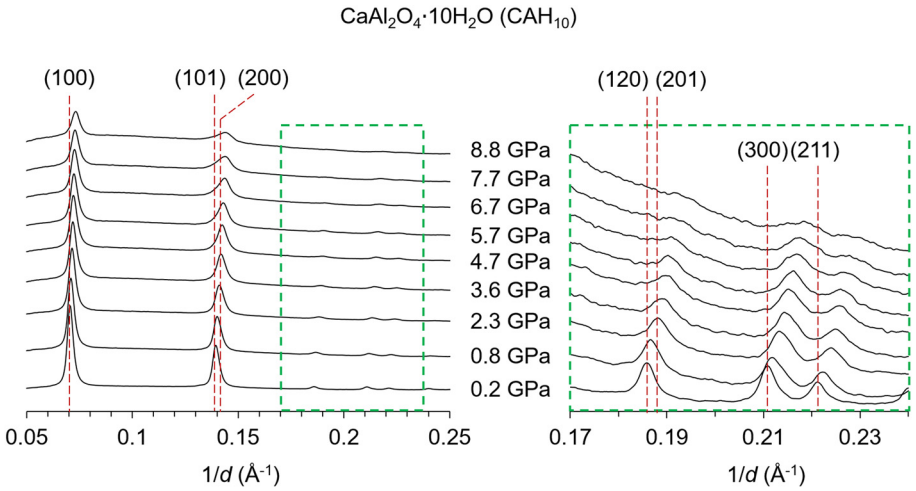

Fig. 2. The diffractograms of CAH_{10} measured under increasing hydrostatic pressure. The green dashed square magnifies the diffraction with $1/d$ between 0.17 and 0.25 $Å^{-1}$. (For interpretation of the references to color in this figure legend, the reader is referred to the web version of this article.)

Table 2
The interplanar *d*-spacings, the lattice parameters (*a* and *b*) and unit cell volume *V*, of CAH_{10} under elevated hydrostatic pressure values. The angles α and β are both fixed at 90°, and γ at 120°.

P (GPa)	Interplanar *d*-spacings (Å)			$d_{(100)}/d_{(200)}$	Refined lattice parameters (Å)				*V* (Å^3)	V_{error} (Å^3)
	(100)	(101)	(200)		*a*	*c*	a_{error}	c_{error}		
0.2	14.207	7.179	7.141	1.99	16.45	8.31	0.04	0.01	1947.5	11.9
0.8	14.130	7.151	7.115	1.99	16.37	8.28	0.06	0.01	1922.7	15.8
2.3	14.016	7.101	7.059	1.99	16.24	8.23	0.06	0.01	1879.5	15.9
3.6	13.950	7.060	7.013	1.99	16.15	8.18	0.04	0.01	1847.5	11.7
4.7	13.896	7.029	7.001	1.99	16.11	8.14	0.06	0.01	1828.2	16.1
5.7	13.848	7.006	6.965	1.99	16.04	8.11	0.05	0.01	1807.8	12.6
6.7	13.784	6.968	6.899	2.00	15.92	8.07	0.01	0.00	1773.4	2.3
7.7	13.752	6.963	6.888	2.00	15.89	8.07	0.01	0.00	1765.8	3.7

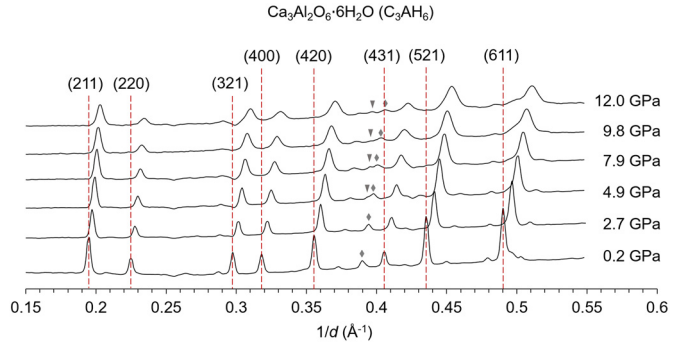

Fig. 3. The diffractograms of C_3AH_6 measured under increasing hydrostatic pressure. The diamond symbol and inversed triangle symbol indicate the split of an overlapped diffraction from C_3AH_6 and ruby (Al_2O_3), respectively.

axial shortening of C_3AH_6 as shown in Fig. 4(a). Such discontinuity on the ε_V vs. pressure plot usually implies a phase transition, [24] as is also observed in previous work [27,28]. By fitting the low pressure data points, the bulk modulus of the ambient-pressure C_3AH_6 structure is 66 ± 2 GPa, comparable to the reported values [25,26]. When fitting the BM-EoS of the high pressure C_3AH_6 phase, we use Eq. (1) and allow both V_0 and K_0 to be refined, as shown in the inset in Fig. 4(d). They are refined to be 2007 ± 27 Å^3 and 70 ± 10 GPa, respectively. Apart from the relatively large uncertainty, the K_0 for high-pressure polymorph of C_3AH_6 is slightly larger than that of the ambient pressure phase.

4. Discussion

1.1 Phase transition of C_3AH_6

On the ε_V vs. pressure plot of C_3AH_6 (Fig. 4(c)), a discontinuity is observed at pressure between ~5 and ~8 GPa, which is most likely due to a phase transition. However as shown in Fig. 3, the diffractogram of C_3AH_6 exhibit a continuous change as pressure increases up to 12 GPa,

Table 3
The interplanar *d*-spacings, the lattice parameter *a* and unit cell volume *V*, of C_3AH_6 under elevated hydrostatic pressure values. All lattice angles are fixed at 90°.

P (GPa)	Interplanar d-spacings (Å)								Refined lattice parameter (Å)		*V* (Å^3)	V_{error} (Å^3)
	(211)	(220)	(321)	(400)	(420)	(431)	(521)	(611)	*a*	a_{error}		
0.2	3.978	4.594	6.077	6.497	7.266	8.282	8.899	10.024	12.58	0.01	1988.6	4.3
2.7	4.028	4.656	6.159	6.583	7.361	8.393	9.016	10.148	12.41	0.01	1912.5	4.2
4.9	4.065	4.695	6.213	6.633	7.42	8.467	9.094	10.233	12.31	0.02	1864.2	6.8
7.9	4.098	4.731	6.260	6.69	7.474	8.533	9.164	10.312	12.22	0.01	1824.8	6.1
9.8	4.116	4.746	6.286	6.721	7.515	8.576	9.206	10.366	12.16	0.01	1798	5.4
12	4.144	4.786	6.332	6.773	7.574	8.627	9.280	10.443	12.07	0.01	1757.7	2.2

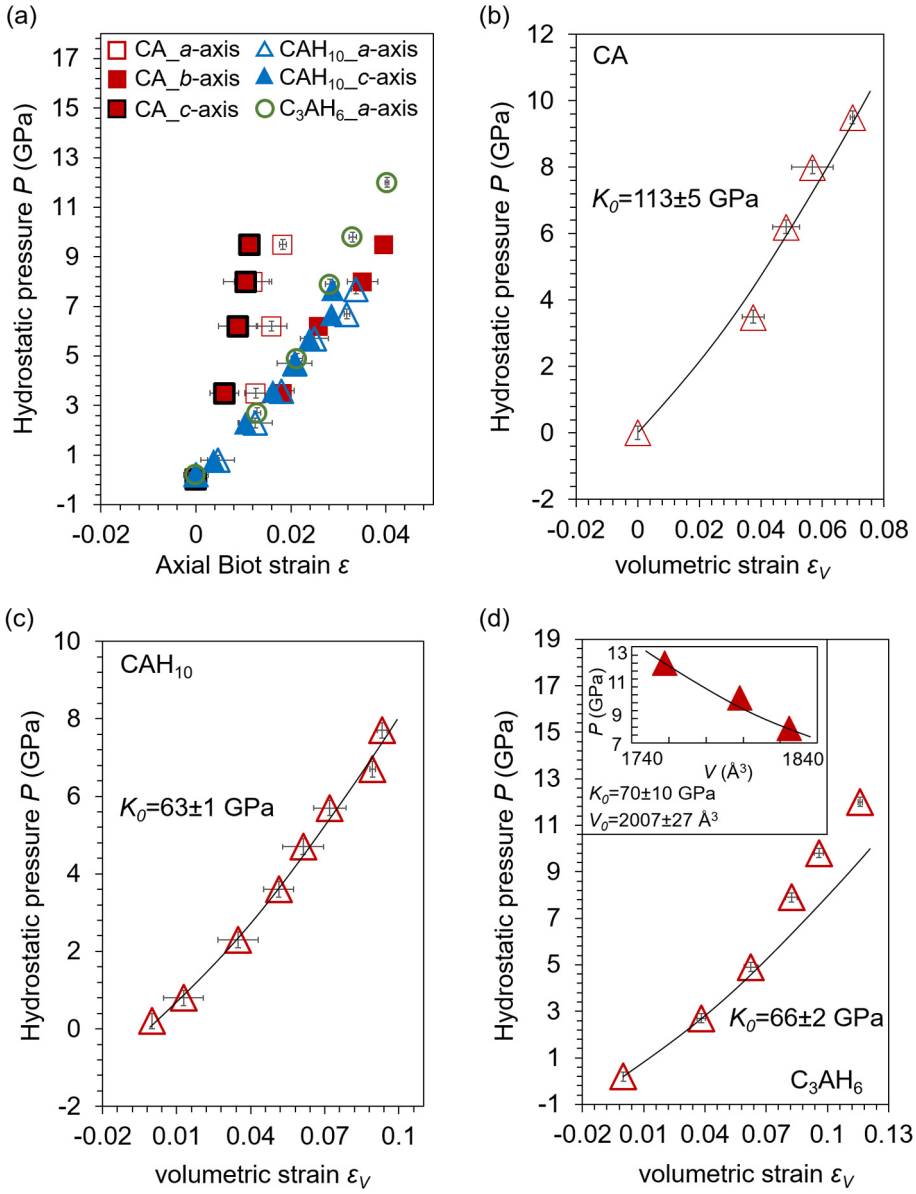

Fig. 4. The hydrostatic pressure plotted as a function of (a) the shortening of each axis of the studied minerals, and the volumetric strains of (b) CA, (c) CAH_{10} and (d) C_3AH_6 crystals. The black curves in (b)-(d) are the fitted second-order Birch-Murnaghan equation of state (BM-EoS), with the bulk modulus K_0 also labeled in the plots. The inset in (d) is the BM-EoS fitting of the high pressure polymorph, where V_0 is allowed to be refined.

with the absence of new peak being generated. Therefore this transformation is not likely a reconstructive phase change that significantly alters the crystal structure, but rather a slight displacement of atom positions which does not require bonds to be disconnected and reconnected [45]. This pressure-induced displacive phase transition is often observed in minerals with (alumino)silicate tetrahedra framework [44,46]. This phase change does not seem to significantly change the bulk modulus.

Similar conclusions were also drawn in previous studies that the phase transition is through the slight displacement of Ca and Al atoms, which enables a few new diffractions that are forbidden by the original *Ia3d* symmetry [27,28]. These new diffraction peaks are very weak, [27] and are not observed in the current study probably due to the pressure-induced peak broadening. $Ca_3Al_2(SiO_4)_3$ (grossular) is a structural analogue of C_3AH_6 where all the (O_4H_4) tetrahedra are replaced by the SiO_4 tetrahedra. As a result, the ambient pressure bulk modulus of $Ca_3Al_2(SiO_4)_3$ is ~2.5 times that of C_3AH_6, since the (O_4H_4) tetrahedron is much more compressive than the SiO_4 tetrahedron [25].

4.1. Correlation between bulk modulus and mineral density

It is widely accepted that the macro-scale stiffness of a cement-based matrix largely depends on the porosity, or equivalently the density of the matrix. This correlation is also validated at microscale, that the packing density of nanoparticles determines the hardness measured by nano-indentation [47]. Is this still valid at the molecular level, i.e. is the stiffness of a single cement-based phase positively proportional to its density? The reported studies seem to indicate that this hypothesis is valid with calcium silicate hydrates (C-S-H), the principal binding phase in hydrated Portland cement. Geng et al. [21] demonstrated that the bulk modulus of C-S-H is dominated by the shortening and densification of the interlayer spacing, rather than the linkage of the silicate tetrahedral chain. Dharmawardhana et al. [48,49] also proposed that the total bond order density (TBOD) is an ideal overall metric for assessing crystal cohesion of C-S-H and anhydrous calcium silicates. Bauchy et al. [50,51] reported that, similar as glass material with topological network, the stiffness of C-S-H is dominated by the average number of constraints that one atom bears from its neighbor atoms.

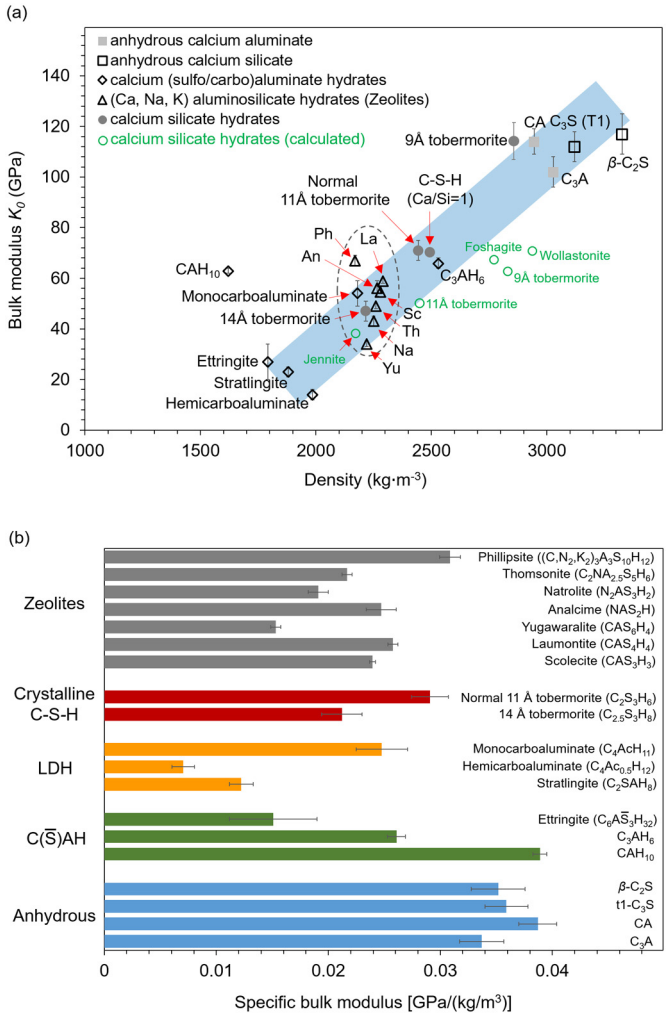

Fig. 5. (a) The bulk moduli K_0 as functions of densities, and (b) the specific bulk moduli (K_0 divided by density ρ), of several cement-based minerals and zeolites. The blue band in (a) indicates the linear trend (experimental data) of K_0 increasing along with ρ. The abbreviations in (a) are Ph (phillipsite), La (laumontite), An (analcime), Sc (scolecite), Th (thomsonite), Na (natrolite), Yu (yugawaralite). The abbreviations in (b) are C (CaO), S (SiO_2), H (H_2O), N (NaO), K (KaO), S̄ (SO_3), c (CO_2). The data are from the current study and previous reports [20,22–24,27,46,52,54,55,59]. (For interpretation of the references to color in this figure legend, the reader is referred to the web version of this article.)

In order to examine the density-driven stiffening hypothesis among the calcium aluminate (hydrates), and other cement-based materials, we plot their bulk moduli as a function of their densities; see Fig. 5(a). The data are from the nano-indentation, HP-XRD and molecular simulations reported in the past two decades [20,22–27,52–60]. The plot also contains the data of a few zeolites as they have similar chemical compositions and crystal structures with cement-based phases [46]. In general, a positive correlation between the density and bulk modulus is observed, as indicated by the blue band in Fig. 5(a). The calcium (sulfo/carbo)aluminate hydrates with LDH (layer-double-hydroxide) structure exhibit relatively lower density ($< 2000\ kg{\cdot}m^{-3}$) and smaller bulk moduli (< 30 GPa), with the exception of monocarboaluminate. The anhydrous calcium aluminates/silicates are the densest ($\rho > 3000\ kg{\cdot}m^{-3}$) and stiffest phases ($K_0 > 100$ GPa) in cement-based composites. The nanocrystalline C-S-H, tobermorite group minerals, C_3AH_6 and zeolite minerals are of intermediate densities and bulk moduli. Molecular calculations (green circle in Fig. 5(a)) also reproduced the density-driven trend, although the values are smaller than experimental data.

We further calculated the specific bulk moduli, i.e. bulk modulus K_0 divided by density ρ, of the experimental studied phases, as shown in Fig. 5(b). Apart from the generally linear correlation between density and bulk modulus, there exist three obvious contradictions: 1) CAH_{10} has the highest specific bulk modulus over all hydrate minerals, and is a complete outliner of the linear trend (blue band in Fig. 5(a)); 2) the zeolite minerals are of similar density, but their bulk moduli vary in a broad range between 30 and 70 GPa; 3) the specific moduli of LDH minerals and calcium (sulfo)aluminate hydrates varies significantly. These contradictions indicate that, the bulk moduli of cement-based minerals are not solely determined by their density. Large numbers of studies in geophysics have demonstrated that, the elastic moduli of minerals with network of rigid units (e.g. SiO_4 and AlO_4 tetrahedra) depend greatly on the topology of the network [44,46]. Under hydrostatic pressure, the corner-shared tetrahedra tend to tilt to accommodate the compression, instead of the rigid bonds (e.g. Si—O and Al—O) being compressed. When the tilting is not permitted by the symmetry of the topology, the mineral normally develops high stiffness.

We compared the topology of CAH_{10} framework with two other minerals in Fig. 6. CAH_{10} has an interconnected network of AlO_6 octahedra and CaO_8 polyhedra, with water and hydroxyl groups filled within the channels (not displayed in Fig. 6 for a better vision of the network). The basic unit of this framework is a $(Ca_3Al_6O_{36})^{48-}$ superstructure, with a 3-fold axis indicated by the black dashed line in Fig. 6(c). Each basic unit is connected with 6 adjacent basic units through edge-sharing of the AlO_6 octahedra. The shared edges are indicated by the red arrows in Fig. 6(c). Unlike corner-sharing, edge-sharing connection has only one possible tilting direction. The 6-shared edges of the basic structural unit are not in a common plan that is perpendicular to the 3-fold axis. As a result, the tilting of the 6-shared edge will basically result in a breaking-down of the structural unit. Therefore, the network tilting is not an energetically favored deformation path of CAH_{10}. Indeed we observed that CAH_{10} shortens in the same rate along *a*-(*b*-) axis and the *c*-axis, i.e. the whole network shrinks isotropically without a change in the overall shape. This strongly implies that the deformation is through the shortening of atom bonds, which explains the high specific bulk modulus of CAH_{10}.

On the contrary, ettringite has rigid calcium aluminate columns but they are not interconnected. The LDH (strätlingite, hemicarboaluminate) minerals only have rigid planer network yet again there exists no rigid connection between the layers. Under hydrostatic pressure, neither the rigid column in ettringite, nor the layer structure in LDH would support the whole structure from shrinking. Meanwhile large quantities of volumetric strain are expected within the water-filled region between these rigid parts, as the hydrogen bond network is much weaker than the primary bonds [27,28,44,58]. As a result, ettringite and LDH minerals exhibit smaller bulk moduli.

It should be noted that the monocarboaluminate is significantly stiffer than strätlingite and hemicarboaluminate, although they share the same LDH structure. The increasing content of carbonate groups in the interlayer regions seems to have a significant influence on the overall stiffness of monocarboaluminate. Besides, the local negative correlation between density and stiffness for ettringite, strätlingite and hemicarboaluminate, also mismatches the overall positive trend. Similar observation is reported for zeolites, that the bulk modulus also depends on the bonding between the host zeolitic framework and the stuffed guest species [46]. Future molecular scale calculation on these cement-based minerals may provide detailed evidence.

5. Conclusions

The current work systematically probes the anisotropic incompressibility and bulk moduli of the major component minerals in calcium aluminate hydration system, using synchrotron-radiation-based HP-XRD. The main conclusions are summarized as follows:

1. The bulk moduli K_0 of CA and CAH_{10} are, for the first time, reported to be 113 ± 5 GPa and 63 ± 1 GPa, respectively. Under

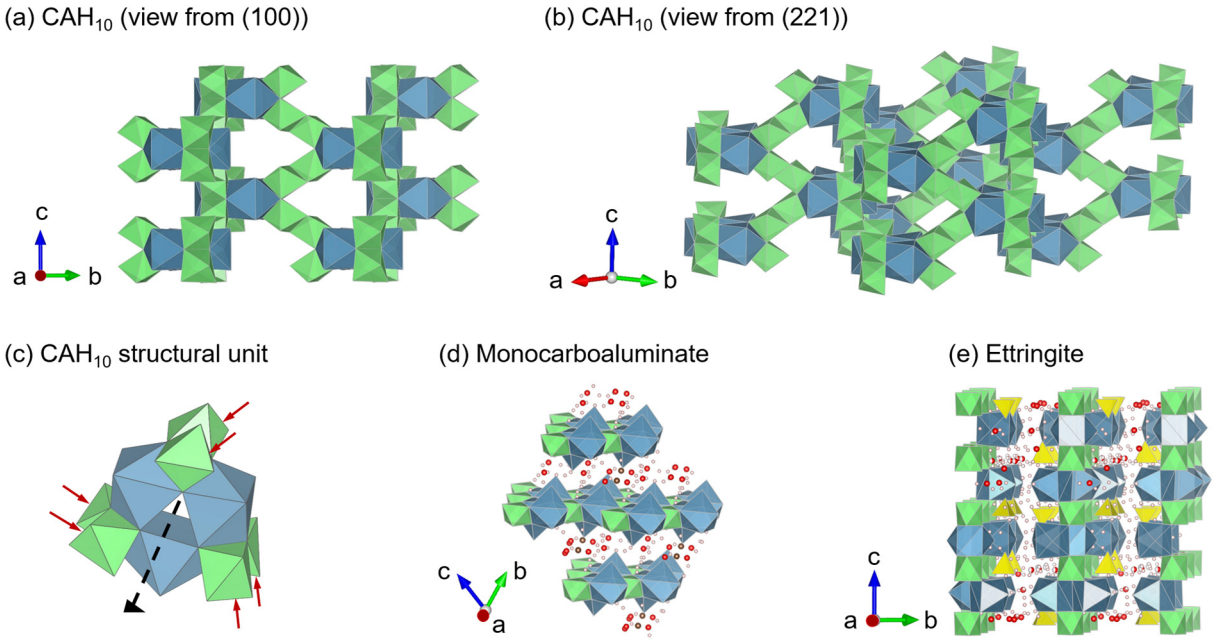

Fig. 6. The topological structure of CaO_8 polyhedra (blue), AlO_6 octahedra (green) and SO_4 tetrahedra (yellow) in (a)–(c) CAH_{10}, (d) monocarboaluminate and (e) ettringite. The black dash in (c) indicates the 3-fold rotation axis. The red, brown and pink spheres are oxygen, carbon and hydrogen atoms, respectively. For viewing convenience, the water and hydroxyl groups in CAH_{10} are not displayed. The visualization is achieved with VESTA package [61]. (For interpretation of the references to color in this figure legend, the reader is referred to the web version of this article.)

hydrostatic pressure, CA crystal develops anisotropic deformation, with the most shortening observed along the *b*-axis, and the least shortening long the *c*-axis. Although the crystal structure of CAH_{10} is anisotropic (hexagonal), it has rather isotropic incompressibilities. A phase transition of C_3AH_6 is observed at pressure between 5 and 8 GPa. The K_0 of the ambient pressure C_3AH_6 phase is 66 ± 2 GPa, and 70 ± 10 GPa for the high pressure polymorph.

2. The bulk moduli of cement-based minerals are, in general, proportional to their densities. However the topological structure of the tetrahedra, octahedra and polyhedra framework has a big influence on the incompressibility of the minerals. When bond-angle-tilting is inhibited in the framework deformation, the mineral may develop a high stiffness even its density is low. One such example is CAH_{10}.
3. This work adds knowledge to understand the mechanical property of single cement-based crystalline phase. It also provides fundamental input for the multiscale homogenization modeling of the mechanical property of calcium aluminate hydration system.

Acknowledgement

This work is funded by the Republic of Singapore's National Research Foundation through a grant to the Berkeley Education Alliance for Research in Singapore (BEARS) for the Singapore-Berkeley Building Efficiency and Sustainability in the Tropics (SinBerBEST) Program. The Advanced Light Source is supported by the Director, Office of Science, Office of Basic Energy Sciences, of the U.S. Department of Energy under Contract No. DE-AC02-05CH11231. Sample preparation of his research was partially supported by COMPRES, the Consortium for Materials Properties Research in Earth Sciences under NSF Cooperative Agreement EAR 1606856. Guoqing Geng acknowledges additional support through the Chinese Scholarship Council (file No. 201206090127).

References

[1] P.K. Mehta, P.J.M. Monteiro, Concrete Microstructure, Properties, and Materials, 4th edition, McGraw-Hill Companies, New York City, 2014.
[2] P. Barnes, J. Bensted, Structure and Performance of Cements, CRC Press, Boca Raton, 2002.
[3] H. Pöllmann, Calcium aluminate cements – raw materials, differences, hydration and properties, Rev. Mineral. Geochem. 74 (2012) 1–82.
[4] K.L. Scrivener, J.L. Cabiron, R. Letourneux, High-performance concretes from calcium aluminate cements, Cem. Concr. Res. 29 (1999) 1215–1223.
[5] Concrete Society, Calcium Aluminate Cement in Construction, A Re-assessment. Technical Report. No. 46, Concrete Society, Slough, 1997.
[6] W.E. Lee, W. Vieira, S. Zhang, K.G. Ahari, H. Sarpoolaky, C. Parr, Castable refractory concretes, Int. Mater. Rev. 46 (2001) 145–167.
[7] S. Rashid, P. Barnes, J. Bensted, X. Turrillas, Conversion of calcium aluminate cement hydrates re-examined with synchrotron energy-dispersive diffraction, J. Mater. Sci. Lett. 13 (1994) 1232–1234.
[8] R.N. Edmonds, A.J. Majumdar, The hydration of monocalcium aluminate at different temperatures, Cem. Concr. Res. 18 (1998) 311–320.
[9] T.R. Jensen, A.N. Christensen, J.C. Hanson, Hydrothermal transformation of the calcium aluminum oxide hydrates $CaAl_2O_4{\cdot}10H_2O$ and $Ca_2Al_2O_5{\cdot}8H_2O$ to $Ca_3Al_2(OH)_{12}$ investigated by *in situ* synchrotron X-ray powder diffraction, Cem. Concr. Res. 35 (2005) 2300–2309.
[10] G. Geng, J. Li, Y.S. Yu, D.A. Shapiro, D.A.L. Kilcoyne, P.J.M. Monteiro, Nanometer-resolved spectroscopic study reveals the conversion mechanism of $CaO{\cdot}Al_2O_3{\cdot}10H_2O$ to $2CaO{\cdot}Al_2O_3{\cdot}8H_2O$ and $3CaO{\cdot}Al_2O_3{\cdot}6H_2O$ at an elevated temperature, Cryst. Growth Des. 8 (2017) 4246–4253.
[11] G. Geng, R.J. Myers, A.L. Kilcoyne, J. Ha, P.J. Monteiro, Ca $L_{2,3}$-edge near edge X-ray absorption fine structure of tricalcium aluminate, gypsum, and calcium (sulfo) aluminate hydrates, Am. Mineral. 102 (2017) 900–908.
[12] O. Bernard, F.J. Ulm, E. Lemarchand, A multiscale micromechanics-hydration model for the early-age elastic properties of cement-based materials, Cem. Concr. Res. 33 (2003) 1293–1309.
[13] F.J. Ulm, G. Constantinides, F.H. Heukamp, Is concrete a poromechanics materials?—a multiscale investigation of poroelastic properties, Mater. Struct. 37 (2004) 43–58.
[14] B. Pichler, C. Hellmich, J. Eberhardsteiner, Spherical and acicular representation of hydrates in a micromechanical model for cement paste: prediction of early-age elasticity and strength, Acta Mech. 203 (2009) 137–162.
[15] P. Gu, J.J. Beaudoin, E.G. Quinn, R.E. Myers, Early strength development and hydration of ordinary Portland cement/calcium aluminate cement pastes, Adv. Cem. Based Mater. 6 (1997) 53–58.
[16] T.J. Chotard, A. Smith, D. Rotureau, D. Fargeot, C. Gault, Acoustic emission characterisation of calcium aluminate cement hydration at an early stage, J. Eur. Ceram. Soc. 23 (2003) 387–398.
[17] E. Nonnet, N. Lequeux, P. Boch, Elastic properties of high alumina cement castables from room temperature to 1600 °C, J. Eur. Ceram. Soc. 19 (1999) 1575–1583.
[18] C. Parr, F. Simonin, B. Touzo, C. Wohrmeyer, B. Valdelièvre, A. Namba, The impact of calcium aluminate cement hydration upon the properties of refractory castables, J. Tech. Assoc. Refract. Jpn. 25 (2005) 78–88.
[19] S. Enzo, G. Fagherazzi, A. Benedetti, S. Polizzi, A profile-fitting procedure for analysis of broadened X-ray diffraction peaks. I. Methodology, J. Appl. Cryst. 21 (1988) 536–542.
[20] G. Geng, R.J. Myers, J. Li, R. Maboudian, C. Carraro, D.A. Shapiro, P.J.M. Monteiro,

Aluminum-induced dreierketten chain cross-links increase the mechanical properties of nanocrystalline calcium aluminosilicate hydrate, Sci. Rep. 7 (2017) 44032.
[21] G. Geng, R.J. Myers, M.J.A. Qomi, P.J.M. Monteiro, Densification of the interlayer spacing governs the nanomechanical properties of calcium-silicate-hydrate, Sci. Rep. 7 (2017) 10986.
[22] J.E. Oh, S.M. Clark, H.R. Wenk, P.J.M. Monteiro, Experimental determination of bulk modulus of 14 Å tobermorite using high-pressure synchrotron X-ray diffraction, Cem. Concr. Res. 42 (2012) 397–403.
[23] J. Moon, J.E. Oh, M. Balonis, F.P. Glasser, S.M. Clark, P.J.M. Monteiro, High-pressure study of low compressibility tetracalcium aluminum carbonate hydrates $3CaO{\cdot}Al_2O_3{\cdot}CaCO_3{\cdot}11H_2O$, Cem. Concr. Res. 42 (2012) 105–110.
[24] J. Moon, J.E. Oh, M. Balonis, F.P. Glasser, S.M. Clark, P.J.M. Monteiro, Pressure induced reactions amongst calcium aluminate hydrate phases, Cem. Concr. Res. 41 (2011) 571–578.
[25] H. Olijnyk, E. Paris, C.A. Geiger, G.A. Lager, Compressional study of katoite [$Ca_3Al_2(O_4H_4)_3$] and grossular garnet, J. Geophys. Res. Solid Earth 96 (1991) 14313–14318.
[26] R.H. Nobes, E.V. Akhmatskaya, V. Milman, B. Winkler, C.J. Pickard, Structure and properties of aluminosilicate garnets and katoite: an ab initio study, Comput. Mater. Sci. 17 (2000) 141–145.
[27] G.A. Lager, R.T. Downs, M. Origlieri, R. Garoutte, High-pressure single-crystal X-ray diffraction study of katoite hydrogarnet: evidence for a phase transition from Ia3d → I-43d symmetry at 5 GPa, Am. Mineral. 87 (2002) 642–647.
[28] G.A. Lager, W.G. Marshall, Z. Liu, R.T. Downs, Re-examination of the hydrogarnet structure at high pressure using neutron powder diffraction and infrared spectroscopy, Am. Mineral. 90 (2005) 639–644.
[29] F. Guirado, S. Galí, S. Chinchón, J. Rius, Crystal structure solution of hydrated high-alumina cement from X-ray powder diffraction data, Angew. Chem. Int. Ed. 37 (1998) 72–75.
[30] A.N. Christensen, B. Lebech, D. Sheptyakov, J.C. Hanson, Structure of calcium aluminate decahydrate ($CaAl_2O_4{\cdot}10D_2O$) from neutron and X-ray powder diffraction data, Acta Crystallogr. Sect. B: Struct. Sci. 63 (2007) 850–861.
[31] G.A. Lager, T. Armbruster, J. Faber, Neutron and X-ray diffraction study of hydrogarnet $Ca_3Al_2(O_4H_4)_3$, Am. Mineral. 72 (1987) 756–765.
[32] S. Ito, K. Suzuki, M. Inagaki, S. Naka, High pressure modifications of $CaAl_2O_4$ and $CaGa_2O_4$, Mater. Res. Bull. 15 (1980) 925–932.
[33] B. Lazić, V. Kahlenberg, J. Konzett, R. Kaindl, On the polymorphism of $CaAl_2O_4$—structural investigations of two high pressure modifications, Solid State Sci. 8 (2007) 589–597.
[34] L. Palacios, S. Bruque, M.A. Aranda, Structure of gallium-doped mayenite and its reduction behavior, Phys. Status Solidi 245 (2008) 666–672.
[35] C. Ma, A.R. Kampf, H.C. Connolly, J.R. Beckett, G.R. Rossman, S.A.S. Smith, D.L. Schrader, Krotite, $CaAl_2O_4$, a new refractory mineral from the NWA 1934 meteorite, Am. Mineral. 96 (2011) 709–715.
[36] M. Kunz, A.A. MacDowell, W.A. Caldwell, D. Cambie, R.S. Celestre, E.E. Domning, R.M. Duarte, A.E. Gleason, J.M. Glossinger, N. Kelez, D.W. Plate, A beamline for high pressure studies at the Advanced Light Source with a superconducting bending magnet as the source, J. Synchrotron Radiat. 12 (2005) 650–658.
[37] I. Kantor, V. Prakapenka, A. Kantor, P. Dera, A. Kurnosov, S. Sinogeikin, N. Dubrovinskaia, L. Dubrovinsky, BX90: a new diamond anvil cell design for X-ray diffraction and optical measurements, Rev. Sci. Instrm. 83 (2012) 125102.
[38] G.J. Piermarini, S. Block, J.D. Barnett, R.A. Forman, Calibration of the pressure dependence of the *R*1 ruby fluorescence line to 195 kbar, J. Appl. Phys. 46 (1975) 2774–2780.
[39] C. Prescher, V.B. Prakapenka, DIOPTAS: a program for reduction of two-dimensional X-ray diffraction data and data exploration, High Pressure Res. 35 (2015) 223–230.
[40] R.W. Cheary, A.A. Coelho, Programs XFIT and FOURYA, deposited in CCP14 Powder Diffraction Library, Engineering and Physical Sciences Research Council, Daresbury Laboratory, Warrington, England, http://www.ccp14.ac.uk/tutorial/xfit-95/xfit.htm, (1996).
[41] J. Laugier, B. Bochu, CELREF, Version 3, Cell parameter refinement program from powder diffraction diagram, Laboratoire des Matériaux et du Génie Physique, Ecole Nationale Supérieure de Physique de Grenoble (INPG), France, 2002.
[42] F. Birctt, Elasticity and constitution of the Earth's interior, J. Geophys. Res. 57 (1952).
[43] H.R. Wenk, L. Lutterotti, S.C. Vogel, Rietveld texture analysis from TOF neutron diffraction data, Powder Diffract. 25 (2010) 283–296.
[44] C.T. Prewitt, R.T. Downs, High pressure crystal chemistry, Rev. Mineral. 37 (1998) 284–318.
[45] H.R. Wenk, A. Bulakh, Minerals: Their Constitution and Origin, 2nd edition, Cambridge University Press, Cambridge, 2016.
[46] G. Gatta, Does porous mean soft? On the elastic behaviour and structural evolution of zeolites under pressure, Zeitschrift für Kristallographie-Cryst. Mater. 223 (2008) 160–170.
[47] F.J. Ulm, M. Vandamme, C. Bobko, J. Alberto Ortega, K. Tai, C. Ortiz, Statistical indentation techniques for hydrated nanocomposites: concrete, bone, and shale, J. Am. Ceram. Soc. 90 (2007) 2677–2692.
[48] C.C. Dharmawardhana, A. Misra, W.Y. Ching, Quantum mechanical metric for internal cohesion in cement crystals, Sci. Rep. 4 (2014) 7332.
[49] C.C. Dharmawardhana, M. Bakare, A. Misra, W.Y. Ching, Nature of interatomic bonding in controlling the mechanical properties of calcium silicate hydrates, J. Am. Ceram. Soc. 99 (2016) 2120–2130.
[50] M. Bauchy, M.J. Qomi, C. Bichara, F.J. Ulm, R.M. Pellenq, Rigidity transition in materials: hardness is driven by weak atomic constraints, Phys. Rev. Lett. 114 (2015) 125502.
[51] M. Bauchy, B. Wang, M. Wang, Y. Yu, M.J.A. Qomi, M.M. Smedskjaer, C. Bichara, F.J. Ulm, R.M. Pellenq, Fracture toughness anomalies: viewpoint of topological constraint theory, Acta Mater. 121 (2016) 234–239.
[52] K. Velez, S. Maximilien, D. Damidot, G. Fantozzi, F. Sorrentino, Determination by nanoindentation of elastic modulus and hardness of pure constituents of Portland cement clinker, Cem. Concr. Res. 31 (2001) 555–561.
[53] O. Bernard, F.J. Ulm, E. Lemarchand, A multiscale micromechanics-hydration model for the early-age elastic properties of cement-based materials, Cem. Concr. Res. 33 (2003) 1293–1309.
[54] S.M. Clark, B. Colas, M. Kunz, S. Speziale, P.J.M. Monteiro, Effect of pressure on the crystal structure of ettringite, Cem. Concr. Res. 38 (2008) 19–26.
[55] J. Moon, S. Yoon, R.M. Wentzcovitch, S.M. Clark, P.J.M. Monteiro, Elastic properties of tricalcium aluminate from high-pressure experiments and first-principles calculations, J. Am. Ceram. Soc. 95 (2012) 2972–2978.
[56] H. Manzano, J.S. Dolado, A. Ayuela, Elastic properties of the main species present in Portland cement pastes, Acta Mater. 57 (2009) 1666–1674.
[57] M.A. Qomi, K.J. Krakowiak, M. Bauchy, K.L. Stewart, R. Shahsavari, D. Jagannathan, D.B. Brommer, A. Baronnet, M.J. Buehler, S. Yip, F.J. Ulm, Combinatorial molecular optimization of cement hydrates, Nat. Commun. 5 (2014).
[58] D. Hou, H. Ma, Y. Zhu, Z. Li, Calcium silicate hydrate from dry to saturated state: structure, dynamics and mechanical properties, Acta Mater. 67 (2014) 81–94.
[59] H. Manzano, R. González-Teresa, J.S. Dolado, A. Ayuela, X-ray spectra and theoretical elastic properties of crystalline calcium silicate hydrates: comparison with cement hydrated gels, Mater. Constr. 60 (2010) 7–19.
[60] H. Manzano, Atomistic Simulation Studies of the Cement Paste Components. Servicio Editorial de la Universidad del País Vasco/Euskal Herriko Unibertsitatearen Argitalpen Zerbitzua. PhD Thesis, (2009).
[61] K. Momma, F. Izumi, VESTA: a three-dimensional visualization system for electronic and structural analysis, J. Appl. Crystallogr. 41 (2008) 653–658.